A slab model of the Great Salt Lake for regional climate simulation

C. Strong[1], A. K. Kochanski[1], and E. T. Crosman[1]

[1]Department of Atmospheric Sciences, University of Utah, Salt Lake City, Utah, USA

Abstract A slab lake model was developed for the Great Salt Lake (GSL) and coupled to a regional climate model to enable better evaluation of regional effects of projected climate change. The GSL is hypersaline with an area of approximately 4400 km^2, and its notable shallowness (the deeper sections average 6.5–9 m at current lake levels) renders it highly sensitive to climate change. A time-independent (constant) effective mixing depth of approximately 5 m was determined for the GSL by numerically optimizing model-observation agreement, and improvement gained using a time-dependent effective mixing depth assumption was smaller than the uncertainty in the satellite-based observations. The slab model with constant effective mixing depth accounted for more than 97% of the variance in satellite-based observations of GSL surface temperature for years 2001 through 2003. Using a lake surface temperature climatology in place of the lake model resulted in annual mean near-surface air temperature differences that were small ($\sim$10^{-2} K) away from the lake, but differences in annual precipitation downstream reached 3 cm (4.5%) mainly because of enhanced turbulent heat fluxes off the lake during spring. When subjected to a range of pseudo global warming scenarios, the annual mean lake surface temperature increased by 0.8°C per degree of air temperature increase.

1. Introduction

The physical, biological, and chemical properties of lakes are known to respond rapidly to climate change [*Adrian et al.*, 2009], although the thermal response of lakes to atmospheric warming has shown considerable regional variability [e.g., *Austin and Colman*, 2007; *Sahoo and Schladow*, 2008; *Schneider and Hook*, 2010; *Sahoo et al.*, 2013]. The coupling of adequate lake and climate models is necessary to further improve understanding of the impact of lakes on regional climate and the influence of climate change on lake ecosystems [*MacKay et al.*, 2009]. Extensive effort at coupling lake thermodynamic models to regional climate models has occurred over the past 20 years [e.g., *Hostetler et al.*, 1993; *Small et al.*, 1999; *Leon et al.*, 2007; *Notaro et al.*, 2012]. For larger-scale simulations involving coupling to land surface models such as the Community Land Model, the representation of lakes is a rich research field with recent substantial advances [e.g., *Martynov et al.*, 2010; *Subin et al.*, 2012; *Bennington et al.*, 2014]. Lake modeling has been highlighted in several recent journal special issues and sections [e.g., *Mironov et al.*, 2010; *Balsamo et al.*, 2012].

In their default configuration, regional climate models such as the Weather Research and Forecasting (WRF) model [*Skamarock et al.*, 2005] treat lake surface temperatures as boundary conditions prescribed in advance of the simulation, and good results can be obtained by prescribing in situ or remotely sensed lake surface temperatures [e.g., *Zhao et al.*, 2012] for retrospective simulations. For future climate simulations, lack of observational guidance encourages use of a lake model, and models of varying complexity are available for this purpose [e.g., *Goyette et al.*, 2000; *Tsuang et al.*, 2001; *Mironov*, 2008; *Gula and Peltier*, 2012]. Most previous studies have focused on moderately complex lake models for the deeper lakes [*Deng et al.*, 2013]. Modeling efforts for lakes are typically limited by a lack of comprehensive lake bathymetry data and in situ temperature and water clarity profiles for model initialization and validation [*Balsamo et al.*, 2010]. As discussed by *Balsamo et al.* [2010], the effective mixing depth of a lake is a crucial parameter for modeling lake-atmosphere interactions, and global data sets are now being developed to provide variables needed to initialize parameterized lake models for numerical weather prediction [*Kourzeneva et al.*, 2012].

Here, we consider the utility of a parsimonious slab lake model (SLM) to represent the shallow, hypersaline Great Salt Lake (GSL) in a regional climate simulation, and we evaluate the potential importance of temporal variations in the lake's effective depth. We assess the skill of the SLM coupled to WRF, and we use the SLM to numerically seek an observationally informed "optimal" effective depth of the lake. Finally, we exercise
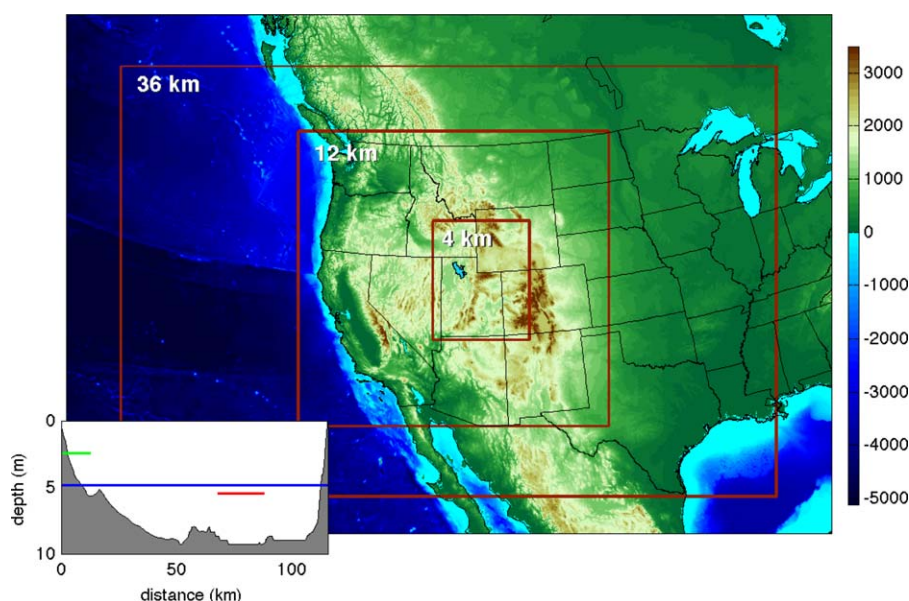
Figure 1. Red rectangles show the boundaries of the nested WRF domains with resolutions increasing inward from 36 km to 12 km and 4 km. The Great Salt Lake is indicated by the blue shading in the 4 km domain. For the inset at lower left, gray shading indicates the bathymetry along the long axis of the Great Salt Lake (transect running northwest-to-southeast), the horizontal blue line is the effective depth optimized for the entire lake (4.8 m), and the green and red horizontal lines show effective depths of 2.5 and 5.5 m optimized for shallow and deep sections of the lake, respectively.

the SLM to evaluate the sensitivity of the lake surface temperature to long-term projected changes in atmospheric temperature and humidity.

The GSL is a terminal lake (no outlets) in the mountainous western United States with a surface elevation approximately 1280 m above sea level (location indicated in Figure 1). The GSL is the largest salt water lake in the Western Hemisphere, with an area of approximately 4400 km^2, and it is notably shallow, with deeper sections averaging 6.5–9 m at current lake levels [*Naftz et al.*, 2013]. The lake is hypersaline (up to eight times as saline as ocean water), and rarely forms ice cover in the current climate. An east-west earthen causeway limits mixing between Gunnison Bay on the northern side (27% salinity) and Gilbert Bay on the southern side (6–15% salinity) [e.g., *Newby*, 1980].

Realistic specification of GSL surface temperatures are important for simulation of projected Wasatch Mountain snowpack because of the GSL's impact on lake effect snow [*Carpenter*, 1993; *Steenburgh et al.*, 2000; *Alcott et al.*, 2012; *Yeager et al.*, 2012]. Accurate GSL surface temperatures are also needed for simulation of climate in adjacent Salt Lake City because lake breeze effects from the GSL account for downstream anomalies in temperature, humidity, and wind [*Zumpfe and Horel*, 2007; *Crosman and Horel*, 2012].

2. Data

We used the MODIS-derived lake surface temperatures from the Terra platform (T_{MODIS}) for 2003 analyzed as in *Crosman and Horel* [2009]. The mean absolute errors of MODIS-derived temperatures as validated against buoy data from 2010 to 2011 were found to be 0.66 K by *Grim et al.* [2013], who conducted a more comprehensive validation than *Crosman and Horel* [2009], who found root mean squared errors of 1.5 K. The nominal solar times for Terra overpasses over the GSL occur at approximately 12:00 A.M. and 12:00 P.M. local solar time. There were 279 available values of lake temperature used for all calculations in 2003 (filled circles, Figure 2a), with nominally as many used for additional validations in 2001 and 2002 (Figures 2b and 2c).

We used monthly GSL elevation data from the National Water Information System [*U.S. Geological Survey*, 2013]. We converted the 2003 elevation time series $z(t)$ to total lake depth $g(t)$ using

$$g(t) = z(t) - z_{ref} + g_{ref} \tag{1}$$

where z_{ref} = 1278.8 m was the lake elevation when a reference depth of g_{ref} = 7.8 m was recorded at a buoy 24 km west of Antelope Island on 25 May 2010 (R. Rowland, personal communication, 2013).
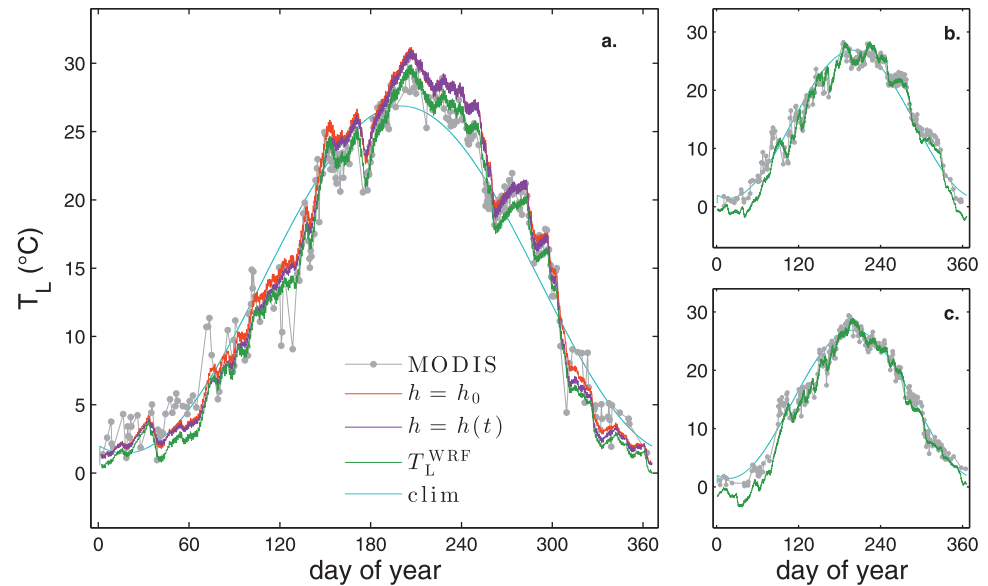
Figure 2. (a) Surface temperature of the Great Salt Lake in 2003 based on MODIS data (section 2), the COARE-SLM framework with constant effective depth ($h = h_0$; section 4.3.1), the COARE-SLM framework with time-dependent effective depth ($h = h(t)$, section 4.3.2), the WRF-SLM framework (T_L^{WRF}, section 3.2), and the [*Crosman and Horel*, 2009] climatology (clim). (b) MODIS, T_L^{WRF}, and clim for 2001. (c) MODIS, T_L^{WRF}, and clim for 2002.

Bathymetric analysis of the GSL [*Baskin and Allen*, 2005; *Baskin and Turner* 2006; *Grim et al.*, 2013] was used to estimate the effective depth averaged over the entire lake, for a shallow portion of the lake, and for a deep portion of the lake (section 4.3.1).

3. Methods

3.1. Slab Lake Model (SLM)

The differential equation used to simulate lake surface temperature (T_L) in the SLM can be written

$$\frac{dT_L}{dt} = -\frac{1}{\rho_w c_w h} F \tag{2}$$

where ρ_w and c_w are the density and specific heat of water, h is the lake's effective depth, and F is the net vertical heat flux at the lake-atmosphere interface defined as positive up (i.e., from lake to atmosphere). This SLM neglects processes not represented by F such as horizontal advection, and has been investigated as a representation of lake and oceanic mixed layers in several studies [e.g., *Ljungemyr et al.*, 1996; *Schneider and Zhu*, 1998].

To account for hypersaline conditions in the GSL, we used $c_w = 3500$ J kg^{-1} K^{-1} and $\rho_w = 1111$ kg m^{-3} [*Sun et al.*, 2008]. We defined F as the linear combination of six vertical fluxes

$$F = F_h + F_e - F_{ld} + F_{lu} - F_{sd} + F_{su} \tag{3}$$

where F_h is upward sensible heat flux, F_e is upward latent heat flux, F_{ld} is downward longwave radiation, F_{lu} is upward longwave radiation, F_{sd} is downward shortwave radiation, and F_{su} is upward shortwave radiation.

3.2. Regional Climate Model Coupled to SLM (WRF-SLM)

We configured and customized WRF Version 3.3.1 to establish our regional climate model (WRF-SLM). Motivated by our interest in accurate simulation of mountain precipitation, we configured WRF following [*Rasmussen et al.*, 2011], meaning we used the Noah land surface model [*Chen and Dudhia*, 2001; *Ek et al.*, 2003],

the Mellor-Yamada-Janjić (MYJ) planetary boundary layer scheme [*Skamarock et al.*, 2005], the Community Atmosphere Model longwave and shortwave schemes [*Collins et al.*, 2006], and the [*Thompson et al.*, 2008] cloud microphysics scheme.

We made three customizations to WRF. First, we encoded the slab lake model described in section 3.1 with $h = 5.1$ m, and ran it separately at grid points defined as part of the GSL. The lake surface temperature simulated by WRF-SLM accounted for at least 97% of the variance observed by MODIS ($r^2 = 0.97$) for each of years 2001 through 2003 (compare green and gray curves, Figure 2). Second, to account for anthropogenic irrigation in urban grid boxes, we introduced a module into the Noah land surface model to prevent volumetric soil moisture in the upper four layers from declining below defined thresholds (ordered from shallowest to deepest, the thresholds levels were 0.095, 0.092, 0.091, and 0.089). This parsimonious empirical adjustment for irrigation effects was inspired by more sophisticated schemes that explicitly track soil moisture deficit [e.g., *Pokhrel et al.*, 2012]. Our soil moisture thresholds were tuned to align WRF's urban latent heat flux (not shown) with available eddy covariance measurements [*Ramamurthy and Pardyjak*, 2011]. Finally, over the GSL, we decreased the saturation vapor pressure from its value over fresh water (q_s) to account for salinity [*Onton and Steenburgh*, 2001]. Following [*Steenburgh and Onton*, 2001], we used 0.70 q_s over the north arm of the lake and 0.94 q_s over the south arm of the lake.

We used a nested domain structure with resolution increasing inward from 36 km to 12 km to 4 km (Figure 1). WRF was forced by 3 hourly atmospheric fields for 2003 from the Climate Forecast System Reanalysis (CFSR) [*Saha et al.*, 2010], and hourly model output was saved including the spatiotemporal evolution of T_L resolved by the SLM. The year 2003 was chosen for primary focus because we had MODIS lake surface temperatures available for this year (section 2), and 2003 is part of the historical climate simulation period (1985–2004) chosen for the CI-WATER project ("Cyberinfrastructure to Advance High Performance Water Resource Modeling"; National Science Foundation award number 1135483). We refer to this simulation as the 2003 WRF-SLM run.

3.3. SLM With Offline Flux Calculations (COARE-SLM)

This subsection describes configurations of the SLM developed to supplement the coupled WRF-SLM framework described in section 3.2. The purpose of these additional frameworks was to provide computational efficiency for effective depth optimization (section 3.3.1) and to evaluate sensitivity of the simulated lake to climate change (section 3.3.2).

3.3.1. COARE-SLM

For computationally efficient numerical optimization of effective depth on eight-core supercomputing nodes, we integrated the SLM offline (i.e., outside of WRF) at 16 WRF grid points equally spaced across the GSL. In this offline SLM framework, turbulent heat fluxes (F_h and F_e) at the lake-atmosphere interface were calculated using bulk parameterizations based on Monin-Obukhov similarity theory (COARE2.6 algorithms) [*Fairall et al.*, 1996], and we refer to this simulation framework as COARE-SLM.

Atmospheric fields needed for the COARE algorithm fluxes (air temperature, air pressure, specific humidity, and wind speed) were taken from the corresponding WRF-SLM coupled run. Upward longwave radiation was calculated from the evolving lake surface temperature as $F_{lu} = \varepsilon \sigma T_L^4$, where $\varepsilon = 0.98$ is the water surface emissivity used in WRF-SLM, $\sigma = 5.67 \times 10^{-8}$ W m^{-2} K^{-4} is the Stefan-Boltzmann constant, and T_L is the simulated lake surface temperature. Remaining radiative fluxes were taken from the WRF-SLM run (F_{ld}, F_{sd}, and F_{su}).

In COARE-SLM, the lake is a prognostic model component and radiative and turbulent fluxes respond to changes in lake surface temperature via the COARE algorithms; the overlying atmosphere is a prescribed boundary condition (taken from the 2003 WRF-SLM run). In WRF-SLM, by contrast, the lake and the overlying atmosphere are both prognostic model components. Results from COARE-SLM and WRF-SLM thus differ, but we find the differences small enough (e.g., compare green and purple curves, Figure 2a) to make COARE-SLM useful for computationally efficient offline optimizations of effective lake depth (section 4.3).

3.3.2. Perturbed COARE-SLM ("Pseudoglobal Warming")

To evaluate the sensitivity of the simulated lake to climate change (section 4.6), we perturbed the COARE-SLM framework as follows. First, we perturbed the hourly near-surface air temperature (T_a) boundary conditions by a constant offset

$$T'_a(t) = T_a(t) + \delta_{T_a}, \tag{4}$$

where the prime denotes perturbed. We perturbed near-surface specific humidity assuming a 7% increase for each K of imposed warming [*O'Gorman and Muller*, 2010]

$$q'(t) = q(t) \cdot (1 + 0.07 \delta_{T_a}). \tag{5}$$

We parameterized the corresponding perturbed downwelling longwave radiation following [*Iziomon et al.*, 2003]

$$F'_{ld}(t) = \sigma T'_a{}^4 \left[1 - \gamma_1 \exp\left(-\gamma_2 \frac{e'}{T'_a} \right) \right] (1 + \gamma_3 N_{tot}^2) \tag{6}$$

where $e'(t)$ is perturbed vapor pressure (hPa) consistent with (4,5), N_{tot} is cloud coverage given in octa, and $\gamma = \{0.29, 0.032, 0.0021\}$ are parameters fit to the 2003 WRF-SLM hourly output. To obtain N_{tot} from the WRF-SLM output, we used maximum-random overlap assumption [*Geleyn and Hollingsworth*, 1979; *Raisanen*, 1998].

4. Results

In this section, we present several analyses of the GSL's effective depth (h) to understand the vertical extent over which fluxes are distributed and to optimize the model-observation agreement. We at first assume h is independent of time, and analyze it via linear regression (section 4.1), harmonic analysis (section 4.2), and numerical optimization (section 4.3.1). We then consider a time-dependent formulation $h = h(t)$, casting it as a numerical optimization in section 4.3.2. We synthesize effective depth results in section 4.4, and we quantify the effect of the slab lake model on regional climate in section 4.5. Finally, in section 4.6, we demonstrate the importance of an explicit lake model by quantifying how lake surface temperature responds to projected climate change.

4.1. Effective Depth From Regression Analysis

First considering a constant effective depth (i.e., no dependence on time; $h = h_0$), we use G to denote the integral of the SLM (2) from an initial time t_0 to time t

$$G \equiv -\frac{1}{\rho_w c_w} \int_{t_0}^{t} F(t') \, dt' = h_0 [T_L(t) - T_L(t_0)]. \tag{7}$$

In this formulation, G is the integrated flux into the lake normalized by $\rho_w c_w$, and depends linearly on the temperature change with coefficient h_0; larger h_0 means a given temperature change requires a larger integrated flux.

We fit the coefficient h_0 in (7) via ordinary least squares linear regression with G as the predictand and $[T_L(t) - T_L(t_0)]$ as the predictor. We defined the net vertical flux ($F(t)$; equation (3)) as the average of corresponding terms from the 2003 WRF-SLM run averaged spatially over the lake, and we used T_{MODIS} as T_L. The time of the first available MODIS observation was used as t_0, and the predictor and predictand were sampled at subsequent values of t for which MODIS data were available. The resulting scatter plot with regression line is shown in Figure 3, with $h_0 = 5.2$ m (Table 1) accounting for 97% of the variance ($r^2 = 0.97$).
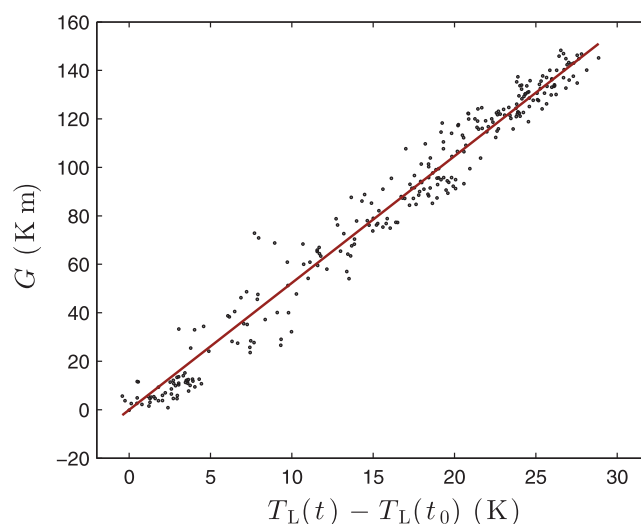

Figure 3. Effective depth cast as the slope of a linear regression (equation (7)) using MODIS lake surface temperatures and normalized integrated fluxes (G) from the 2003 WRF-SLM simulation (details in section 4.1).

4.2. Effective Depth From Harmonic Analysis

To further consider a time-independent effective depth informed

Table 1. Summary of Effective Depths Indicated by Various Analysis Methods[a]

Analysis	Section	Effective Depth	J
Regression analysis	4.1	$h_0 = 5.2$ m	–
Harmonic analysis	4.2	$\bar{h}_{low} = 5.1$ m	–
Optimization entire lake	4.3.1	$h_0 = 4.8$ m	1.84 K
Optimization deep portion	4.3.1	$h_0 = 5.5$ m	1.90 K
Optimization shallow portion	4.3.1	$h_0 = 2.5$ m	2.14 K
Optimization $h = h(t)$	4.3.2	$\bar{c} = 5.5$ m, $c_h = 1.9$ m	1.79 K

[a]The value of the cost function J (equation (12)) is given for the optimization methods.

by data, we construct harmonic approximations of T_L and F

$$\tilde{T}_L(t) = \sum_k a_k \cos\left(2\pi kt/s - \alpha_k\right) + a_0 \tag{8a}$$

$$\tilde{F}(t) = \sum_k b_k \cos\left(2\pi kt/s - \beta_k\right) \tag{8b}$$

where s is the number of seconds per year, F is assumed to have zero mean, and the approximations use harmonics $k = 1, 2, \ldots, K$. Substituting (8) into the SLM (2) and differentiating $\tilde{T}_L$ yields

$$\sum_k \frac{2\pi k a_k}{s} \sin\left(\frac{2\pi kt}{s} - \alpha_k\right) = \sum_k \frac{b_k}{\rho_w c_w h_k} \cos\left(\frac{2\pi kt}{s} - \beta_k\right), \tag{9}$$

where the subscript on h_k indicates that h is allowed to differ among harmonics (i.e., to be frequency dependent).

The derivative in the SLM (2) implies the phase lag

$$\alpha_k = \beta_k - \pi/2, \tag{10}$$

meaning that lake surface temperature increases when the net flux is negative (i.e., into the lake). This lag is apparent in Figure 4 where the F and T_L data from section 4.1 are approximated by (8) with $K = 3$ (chosen arbitrarily to emphasize lower-frequency fluctuations). For the subset of harmonics $\Phi \subset \{1, 2, \ldots, K\}$ satisfying (10), the sine term on the left side of (9) becomes $\cos\left(2\pi kt/s - \beta_k\right)$, yielding the following expression for h_k

$$h_k = \frac{b_k s}{2\pi k \rho_w c_w a_k}; \quad k \in \Phi; \quad a_k \neq 0. \tag{11}$$

Effective depths are shown in Figure 5 for the subset of harmonics that satisfy (10) to within $\pm \pi/5$.

Low frequency fluctuations with periods longer than 1 month ($k \leq 11$; left side of Figure 5) are associated with effective depths between 4 and 7 m, with an average of $\bar{h}_{low} = 5.1$ m (Table 1). High frequency fluctuations with periods shorter than 1 month ($k > 11$; right side of Figure 5) are associated with effective depths averaging 2.7 m. Analytical models for oceanic mixed layers with periodic forcing [e.g., *Price et al.*, 1986; *Shaviv*, 2008] suggest that effective depth is inversely proportional to the square root of the forcing frequency, and the dashed line in Figure 5 shows the fit of this scaling to the GSL data (i.e., $h \propto \eta k^{-1/2}$ where η is a constant). The appearance of large-amplitude submonthly variations in the MODIS lake surface temperature data (Figure 2) is consistent with amplification of short-term variations by shallower effective depths.

4.3. Effective Depth From Numerical Optimization

In this subsection, we approach effective depth as a numerical optimization problem. We consider an effective depth that is constant over time in subsection 4.3.1, and we consider a time-dependent effective depth
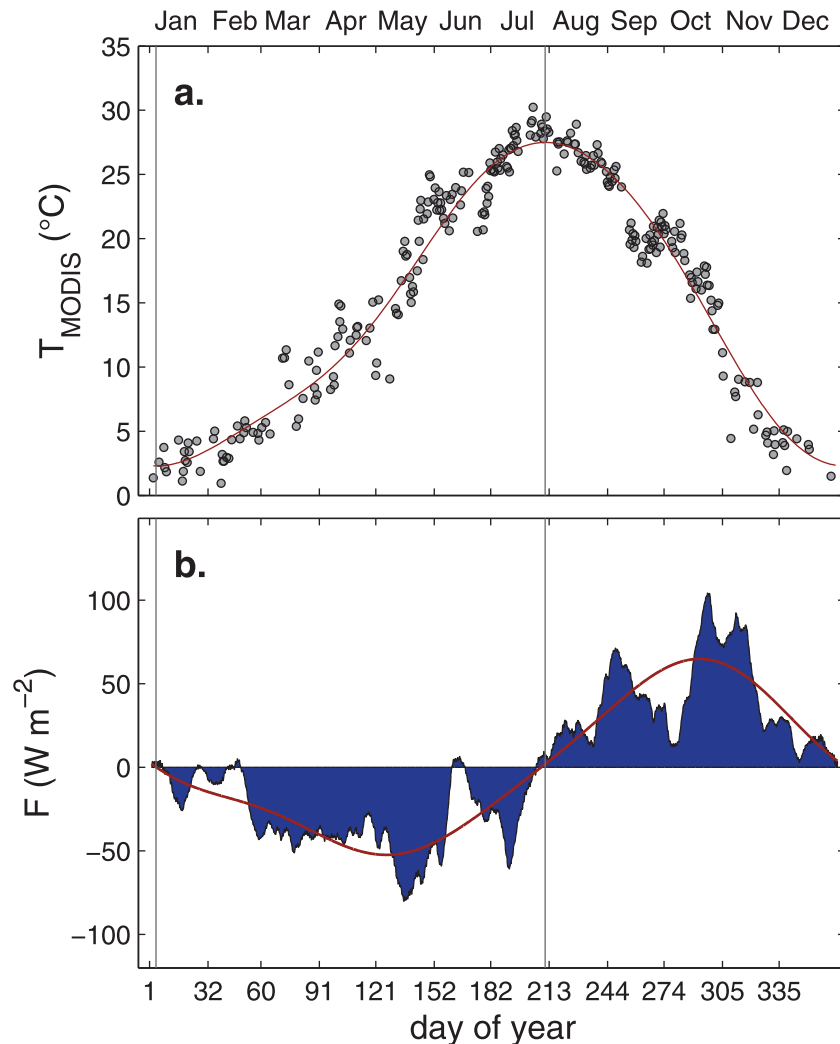
Figure 4. Red curves show harmonic approximations ($K = 3$; equation (8)) of (a) 2003 lake surface temperature from MODIS (filled circles) and (b) net heat flux at the lake-atmosphere interface based on hourly output from the 2003 WRF-SLM run. Net heat fluxes were converted to a 30 day running mean for display only (blue shading). To illustrate phase lag, critical points of T_{MODIS} are indicated by vertical gray lines on each plot.

in subsection 4.3.2. Formally, both problems can be cast in a data assimilation framework, but if we assume no a priori knowledge about the effective depth, this reduces to finding h that minimizes the sum of the squared deviations of the modeled values from the observations [e.g., *Balsamo et al.*, 2010]. To facilitate interpretation of units, we write the associated cost function as a root mean square error

$$J(h) = \left\{ \frac{1}{n_\Gamma} \sum_{t \in \Gamma} \left[T_L^o(t) - T_L^b(t, h) \right]^2 \right\}^{1/2} \tag{12}$$

where T_L^o is the lake surface temperature observed by MODIS, T_L^b is the lake surface temperature simulated by the SLM, and Γ is the set of n_Γ times for which MODIS observations are available. For a given specification of h, we integrated COARE-SLM (section 3.3.1), and used the spatial average of the resulting lake surface temperatures as $T_L^b(t, h)$.

4.3.1. Time-Independent Case for Numerical Optimization
To obtain results corresponding to analyses in sections 4.1 and 4.2, we consider in this subsection a minimization of J assuming that effective depth is a constant (i.e., independent of time; $h = h_0$). We denote this constrained optimization as
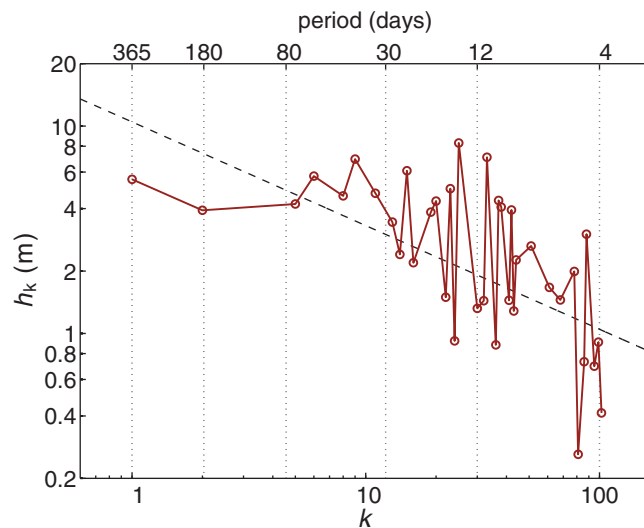
Figure 5. Dependence of effective depth on harmonic integer k (corresponding period length in days is indicated on the upper axis). The dashed line fits effective depth as inversely proportional to the square root of k.

$$\arg \min_{h_0} J(h_0); \text{ subject to : } h_0 \in [0, \infty],$$

$$(13)$$

and obtained the solution numerically using COARE-SLM and an interior-point algorithm [e.g., *Byrd et al.*, 2000]. Figure 6 shows the graph of $J(h_0)$ with a filled circle at $h_0 = 4.8$ m indicating the minimization of J at 1.84 K (Table 1). The lake surface temperature simulated by COARE-SLM for $h_0 = 4.8$ m is shown by the orange curve in Figure 2.

The blue line on the inset in Figure 1 shows how $h_0 = 4.8$ m relates to the bathymetry of the lake depicted along its long axis 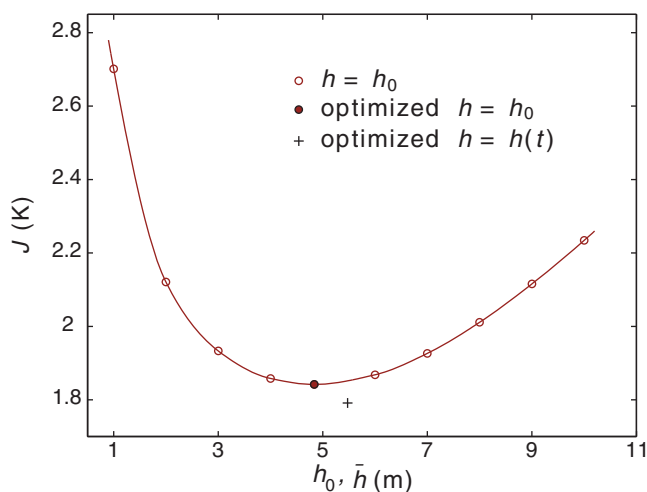(from northwest to southeast). To further probe the reasonableness of this analysis approach, we optimized h_0 as above but for a shallow portion of the lake where depth averages 3.4 m ($41.550° \leq \phi \leq 41.645°$; $-112.942° \leq \lambda \leq -112.803°$), and this yielded $h_0 = 2.5$ m (Table 1; green line on Figure 1 inset). Optimizing h_0 as above but for a portion of the lake where depth averages 8.4 m ($40.133° \leq \phi \leq 40.938°$; $-112.498° \leq \lambda \leq -112.354°$) yielded $h_0 = 5.5$ m (Table 1; red line on Figure 1 inset).

4.3.2. Time-Dependent Case for Numerical Optimization

In this subsection, we seek a minimization of J for a time-dependent effective depth $h = h(t)$ returning to 2003 as our main focus. Based on limited understanding of mixing in the GSL at current lake levels [e.g., *Beisner et al.*, 2009; *Naftz et al.*, 2013], we posited $h(t)$ to evolve as a mean value ($\bar{h}$) plus the first harmonic of the annual cycle

$$h(t) = \bar{h} + c_h \cos\left(\frac{2\pi t}{s} - \phi_h\right)$$

$$(14)$$

as illustrated schematically in Figure 7. We write the associated constrained optimization of $h(t)$ as

$$\arg \min_{\bar{h}, c_h, \phi_h} J(h(t)); \text{ subject to : } \bar{h}, c_h \in [0, \infty]; \bar{h} > c_h,$$

$$(15)$$

where the inequality constraint ensured $h(t) > 0$.

The optimal parameter set was $\{\bar{h} = 5.5 \text{ m}, c_h = 1.9 \text{ m}, \phi_h = 2.3\}$, minimizing J at 1.79 K (Table 1). We show the associated $h(t)$ schematically in Figure 7, and we show the dependence of J on phase (ϕ_h) and amplitude (c_h) for fixed $\bar{h} = 5.5$ m in Figure 8. As amplitude c_h is increased (moving up from lower edge of Figure 8), J decreases slightly for phases that place the maximal effective depth in spring-summer ($\phi_h < \pi$; left half of Figure 8), and J is increased for phases that place the maximal effective depth in fall-winter (right half of Figure 8). By increasing the spring-summer effective depth and decreasing the fall-winter effective depth, the optimal $h(t)$ slowed the warm season increase in T_L and accelerated the cold season decrease in T_L (compare orange and purple curves, Figure 2). The reduction in J achieved by allowing time dependence in the effective depth is only 0.05 K ($J(h_0)$ minimized at 1.84 K and $J(h(t))$ minimized at 1.79 K), and this reduction is an order of magnitude smaller than the mean absolute error of MODIS-derived temperatures (section 2). Morever, we find the time-dependent $h = h(t)$ solution obtained here to be physically implausible, given that deeper effective depths are generally observed over the GSL during the fall-winter [*Crosman and Horel*, 2009]. To significantly enhance model performance, a time-dependent effective depth may need to vary

Figure 6. Dependence of cost function (J; equation (12)) on the effective mixing depth. The circles are connected by a spline curve and indicate discrete values of J for various time-independent effective depths (h_0). The filled circle at $h_0 = 5.1$ m minimizes J. For comparison, the cross indicates the minimization of J by a time-dependent effective depth ($h = h(t)$; equation (14)).

according to the frequency of the forcing (section 4.2) or be influenced by more explicit representation of lake physics (section 4.1).

4.4. Synthesis of Effective Depth Results

The regression analysis (section 4.1) and harmonic analysis (section 4.2) were motivated by the formulation of the SLM (2), and provided data-informed effective depths slightly larger than 5 m (Table 1). Optimizing a time-dependent h using (14) required three parameters yielding a root mean square error of $J = 1.79$ K. The Akaike information criterion slightly favors this three-parameter $h = h(t)$ model over the one-parameter $h = h_0$ model optimized in section 4.3.1 with

$J = 1.84$ K (assuming normally distributed errors with constant variance) [e.g., *Burnham and Anderson*, 2002]. However, as noted above, the 0.05 K reduction in J (filled circle versus cross in Figure 6) is far smaller than the nominal 0.66 K uncertainty associated with the MODIS data we used (section 2). Moreover, the salinity and shortwave penetration dynamics in the GSL are complex, and the currently available profile data [e.g., *Naftz et al.*, 2013] are not adequate to support a physically based argument for why effective depth should maximize during spring-summer.

The regression, harmonic, and optimization analyses summarized immediately above and in the first three rows of Table 1 yield $h_0 \sim 5$ m and were based on atmospheric fields from WRF-SLM with $h_0 = 5.1$ m. We obtained this level of agreement through an iterative procedure (we used an initial guess for h_0 in WRF-SLM, optimized h_0 using COARE-SLM forced by the WRF-S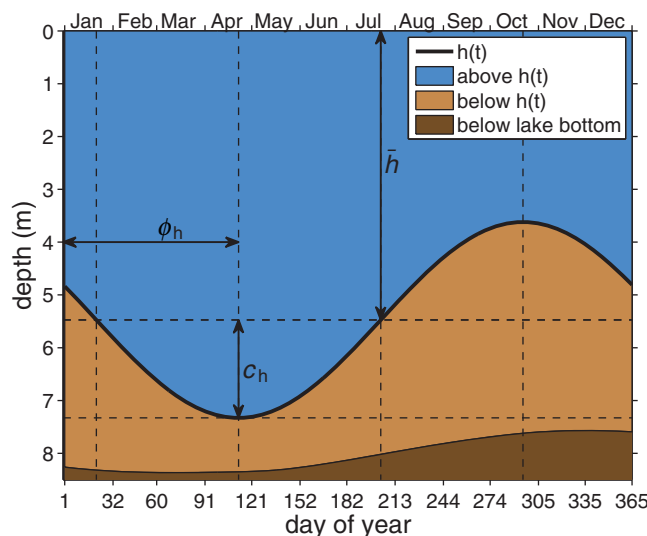LM output, reran WRF-SLM with the new optimized h_0, and then optimized h_0 one more time). The regression, harmonic, and optimization analyses (first three rows, Table 1) were deemed close enough to $h_0 = 5.1$ m that the substantial expense of further iteration with WRF-SLM was not justified. Moreover, the model-observation agreement (cost function $J(h_0)$) was found to change very little over the range $4 \leq h_0 \leq 6$ m (red curve, Figure 6).

Figure 7. Schematic illustrating time-dependent effective mixing depth $h(t)$ with phase ϕ_h, amplitude c_h, and mean $\bar{h}$. The dark brown region lies below the total depth of the lake estimated by equation (1).

4.5. Effects on Regional Climate

To assess the effects of using a lake model as in the WRF-SLM framework, we quantify how regional climate differs in a simulation where we prescribe a climatological annual cycle of lake
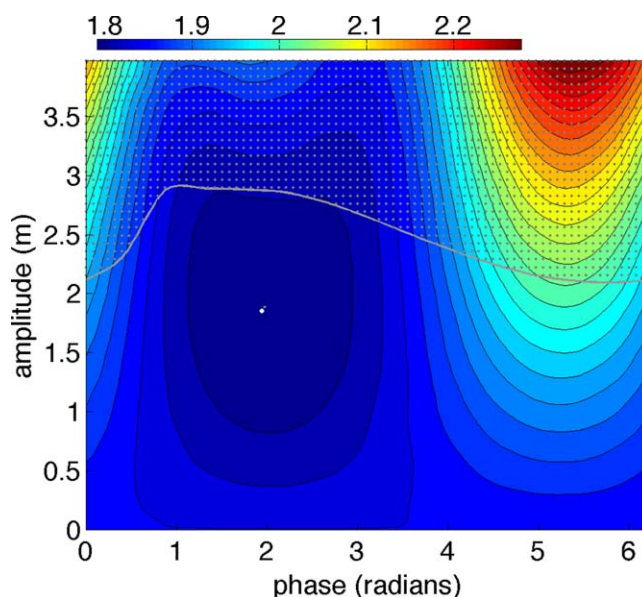
Figure 8. Dependence of cost function (J; equation (12)) on the phase (ϕ_h) and amplitude (c_h) of a time-dependent effective depth ($h(t)$; equation (14)). The open circle is the optimal solution to (15) obtained numerically via the interior-point algorithm. Stippling above the gray contour indicates solutions that would exceed total lake depth (i.e., appear in the dark brown shading in Figure 7) at some point during the annual cycle.

surface temperature (WRF-CLIM). The WRF-SLM simulation was the 2003 case with $h_0 = 5.1$ m, and the WRF-CLIM simulation was a repeat of the 2003 WRF-SLM but with the lake surface temperature prescribed as the annual harmonic from [*Crosman and Horel*, 2009]. The annual harmonic lake surface temperature tended to be warmer than WRF-SLM except during days of year 200–300, and averaged 0.67° K warmer overall. Climatological (clim) and WRF-SLM simulated lake temperature (T_L^{WRF}) are shown in Figure 2a (cyan and green curves, respectively), and their difference is shown by shading in Figure 9a. For calculations here, we consider WRF-SLM to be truth and refer to WRF-CLIM minus WRF-SLM as the "bias" (i.e., bias refers to the difference that arises from using a prescribed lake climatology in place of the SLM).

The bias in daily mean 2 m air temperature (T_2) over the lake (black curve, Figure 9a) was approximately 0.5 times the bias in daily mean lake surface temperature (shading, Figure 9a). In the annual mean, small positive T_2 anomalies (order 10^{-1} °C) can be seen near the GSL and seven small lakes and reservoirs for which we used analogous slab models in the 2003 WRF-SLM run (e.g., Bear Lake just northeast of the dashed box, Figure 9b), and these anomalies decreased to order 10^{-2} °C farther from the water bodies. Downstream to the east and northeast of the GSL, daily mean T_2 anomalies were especially small (red curve, Figure 9a) and averaged close to zero or negative where potential warming was offset in part by positive precipitation biases (compare Figures 9b and 9c). The bias in annual accumulated precipitation reached 3 cm (4.5%) downstream from the lake, and developed primarily during spring (days of year 100–135, green curve in Figure 9a) as lake surface temperature biases approaching $+5$°C enhanced monthly mean turbulent heat fluxes by approximately 50% (enhanced fluxes not shown).

4.6. Response of Slab Lake Model to Projected Climate Change
To further illustrate the importance of having an explicit model of the Great Salt Lake, we quantify the sensitivity of T_L to climate change, considering changes in air temperature and also lake effective depth. We
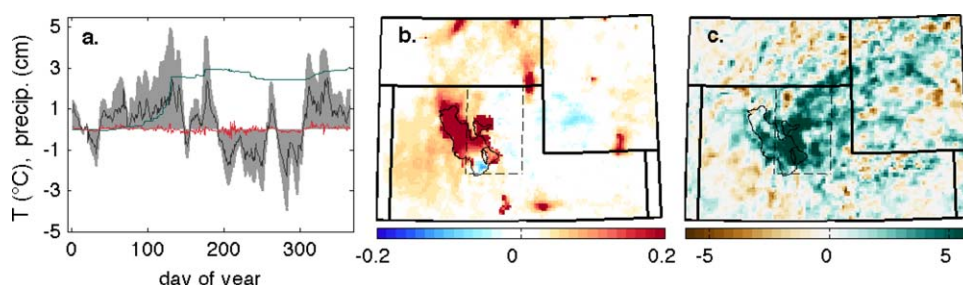

Figure 9. For 2003, comparison of a simulation where lake surface temperatures were prescribed by an annual climatology (WFF-CLIM) to a simulation that used the slab lake model (WRF-SLM). The plotted differences (WRF-CLIM minus WRF-SLM) are: (a) daily mean lake surface temperature (shading), daily mean 2 m air temperature over the lake (black curve), daily mean 2 m air temperature over nonlake portion of dashed box in plot b (red curve), and accumulated precipitation over nonlake portion of dashed box in plot b (green curve). Maps show differences in annual mean (b) 2 m air temperature (°C) and (c) accumulated precipitation (cm).
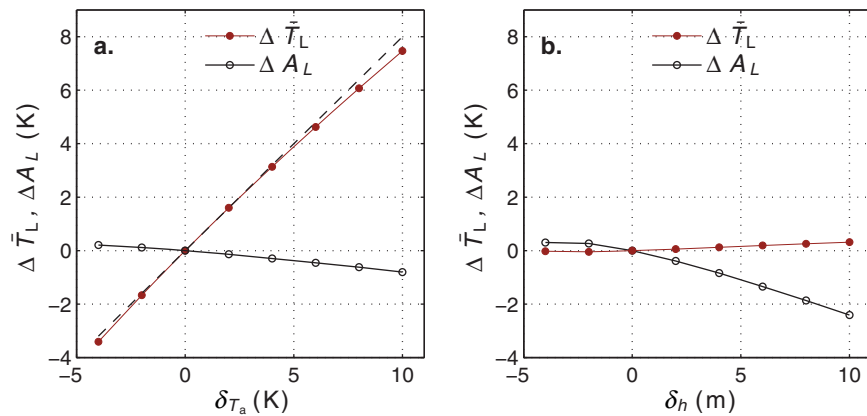
Figure 10. (a) The abscissa indicates air temperature offset (δ_{T_a}) defining a climate perturbation scenario (sections 3.3.2 and 4.6). The ordinate shows the associated change in the annual mean lake surface temperature ($\Delta \bar{T}_L$) and the associated change in the amplitude of the annual cycle of lake surface temperature (ΔA_L). The effective lake depth was held constant at $h_0 = 4.8$ m for this panel. (b) The abscissa indicates a perturbation to the effective lake depth (δ_h), and the ordinate shows the associated $\Delta \bar{T}_L$ and ΔA_L. The climate was kept fixed for this figure ($\delta_{T_a} = 0$).

focus on the annual mean lake surface temperature ($\bar{T}_L$) and the amplitude of the annual mean cycle of lake surface temperature (A_L; calculated by fitting (8) with $K = 3$). We denote the response of these variables to perturbations of air temperature or effective depth as $\Delta \bar{T}_L$ and ΔA_L.

To first test the sensitivity of $\bar{T}_L$ to changes in air temperature, we fixed the lake depth at $h_0 = 4.8$ m following section 4.3.1, and we ran the perturbed COARE-SLM framework as detailed in section 3.3.2 ("pseudoglobal warming"). We exercised this framework using the set of temperature offsets $\delta_{T_a} = \{-4, -2, \ldots, 10\,\text{K}\}$ in (4), and show the resulting change in the annual mean lake surface temperature ($\Delta \bar{T}_L$) using filled red circles in Figure 10a. The associated quadratic polynomial fit shown by the red curve in Figure 10a is

$$\Delta \bar{T}_L(\delta_{T_a}) = a_1 \delta_{T_a}^2 + a_2 \delta_{T_a} + a_3 \tag{16}$$

with parameters $\{a_1 = -7.0 \times 10^{-3}; a_2 = 8.2 \times 10^{-1}; a_3 = -1.3 \times 10^{-2}\}$. Neglecting the quadratic term, (16) indicates that the annual mean lake surface temperature increased by 0.8 K per degree of atmospheric warming (dashed line, Figure 10). For comparison, the larger depths of the Great Lakes yielded a dampened response of approximately 0.6 K per degree of atmospheric warming, despite substantial loss of seasonal ice cover [*Gula and Peltier*, 2012]. Positive δ_{T_a} also reduced the amplitude of the annual cycle of lake surface temperature (ΔA_L, Figure 10a) because the lake warmed slightly faster in the cold season than in the warm season.

In Figure 10b, we fix the temperature perturbation at $\delta_{T_a} = 0$ and introduce an effective lake depth perturbation of $\delta_h = \{-4, -2, \ldots, 10\,\text{m}\}$ (implicit in this sensitivity test is the potential for effective depth to change in response to total lake depth). The amplitude of the annual cycle of lake surface temperature declined with increasing effective lake depth (ΔA_L, Figure 10b). The ΔA_L response to each meter increase in h was approximately three times larger than the ΔA_L response to each K of air temperature increase (compare ΔA_L slopes in Figures 10a and 10b). The response of the annual mean lake temperature to effective depth perturbations was modest ($\Delta \bar{T}_L$, Figure 10b).

5. Summary and Discussion

A slab lake model with an effective depth of approximately 5 m realistically simulated the annual cycle of lake surface temperature for the GSL when coupled to a regional climate model (WRF-SLM), and also when forced by a prescribed atmosphere with offline flux formulations (COARE-SLM). In both frameworks, the slab lake accounted for at least 97% of the lake surface temperature variance based on MODIS data for 2001–2003. Regression analysis of simulated fluxes and observed lake surface temperatures indicated 5.2 m as an effective depth for the lake. Harmonic analysis of the same data indicated effective depths of 4–7 m (average of 5.1 m) for fluctuations with periods longer than a month, and effective depths averaging 2.7 m for fluctuations with periods shorter than a month. Numerically optimizing effective depth, we minimized

the root mean square departure of the model from observations by prescribing a constant (time independent) effective depth of 4.8 m. The reduction in root mean square error in optimizing a time-dependent (harmonic annual cycle) effective depth was smaller than the uncertainty associated with the MODIS surface temperature retrieval.

Using a lake surface temperature climatology in place of the lake model in 2003 resulted in annual mean near-surface air temperature differences that were small ($\sim 10^{-2} \, ^\circ$C) away from the lake, but differences in annual precipitation downstream reached 3 cm (4.5%) mainly because of enhanced springtime turbulent heat fluxes. Analyzing the sensitivity of the lake to climate change, each 1 K of atmospheric warming increased the annual mean lake surface temperature by 0.8 K and decreased the amplitude of the annual mean cycle of lake surface temperature by 0.08 K. Each 1 m increase in effective lake depth had a modest effect on annual mean lake surface temperature, and dampened the annual cycle of lake surface temperature by approximately 0.25 K (dampening smaller than 1%).

We conclude that a slab lake model with an effective depth of approximately 5 m provides a parsimonious and sufficiently realistic representation of the GSL for the purpose of regional climate modeling. These results stem from the shallowness of the GSL, and contrast with investigations of deeper lakes requiring more sophisticated treatment of vertical mixing [e.g., *Gula and Peltier*, 2012]. The GSL physical environment is a highly complex, multifaceted system, the details of which cannot be fully represented by a simple slab model such as that used here. The mixing dynamics of the GSL are impacted by vertical gradients in salinity (dense brine layers near the bottom and freshwater lenses near the surface), seasonal, and interannual fluctuations in inflow from several rivers, and large seasonal variations in the effective penetration of sunlight into the water column associated with changes in algae concentrations [*Crosman and Horel*, 2009; *Beisner et al.*, 2009]. In addition, the areal extent and depth of the GSL is fixed spatially in this study, masking any possible relationship that might exist between lake areal extent, spatially varying depth, and the atmosphere (although we did present a sensitivity analysis to effective lake depth in section 4.6).

The SLM is nonetheless successful in this application because the shallowness of the GSL yields a large-amplitude annual cycle comparable to that of air temperature, overwhelming shorter-term fluctuations driven by more complex processes. These results imply that a simple slab lake model may be applicable for use in regional climate simulations near other large shallow lakes worldwide (e.g., Lake Manitoba in Canada, Lake Urmia in Iran, Lake Mweru in Africa, and Lake Taymyr and Balkhash in Asia).

References

Adrian, R., et al. (2009), Lakes as sentinels of climate change, *Limnol. Oceanogr. Methods*, *54*(6 part 2), 2283–2297.

Alcott, T. I., W. J. Steenburgh, and N. F. Laird (2012), Great Salt Lake-effect precipitation: Observed frequency, characteristics, and associated environmental factors, *Weather Forecasting*, *27*(4), 954–971, doi:10.1175/WAF-D-12-00016.1.

Austin, J. A., and S. M. Colman (2007), Lake Superior summer water temperatures are increasing more rapidly than regional air temperatures: A positive ice-albedo feedback, *Geophys. Res. Lett.*, *34*, L06604, doi:10.1029/2006GL029021.

Balsamo, G., E. Dutra, V. M. Stepanenko, P. Viterbo, P. M. A. Miranda, and D. Mir (2010), Deriving an effective lake depth from satellite lake surface temperature data: A feasibility study with MODIS data, *Borea*, *15*, 178–190.

Balsamo, G., R. Salgado, E. Dutra, S. Boussetta, T. Stockdale, and M. Potes (2012), On the contribution of lakes in predicting near-surface temperature in a global weather forecasting model, *Tellus, Ser. A*, *6415829*, doi:10.3402/tellusa.v64i0.15829.

Baskin, R. L., and D. V. Allen (2005), Bathymetric map of the south part of the Great Salt Lake, Scientific Investigations Map 2894, technical report, U.S. Geol. Surv, Salt Lake City, Utah. [Available at http://pubs.usgs.gov/sim/2005/2894/ last accessed June 19, 2014.]

Baskin, R. L., and J. Turner (2006), Bathymetric map of the north part of the Great Salt Lake, Scientific Investigations Map 2954, technical report, U.S. Geol. Surv, Salt Lake City, Utah. [Available at http://pubs.usgs.gov/sim/2006/2954/, last accessed June 19, 2014.]

Beisner, K., D. L. Naftz, and W. P. Johnson (2009), Evidence and implications of movement of the deep brine layer in the south arm of Great Salt Lake, Utah, *Nat. Resour. Environ. Issues*, *15*, 53.

Bennington, V., M. Notaro, and K. D. Holman (2014), Improving climate sensitivity of deep lakes within a regional climate model and its impact on simulated climate, *J. Clim.*, *27*, 2886–2911. doi:10.1175/JCLI-D-13-00110.1.

Burnham, K. P., and D. R. Anderson (2002), *Model Selection and Multimodel Inference a Practical Information-Theoretic Approach*, Springer, New York.

Byrd, R. H., J. C. Gilbert, and J. Nocedal (2000), A trust region method based on interior point techniques for nonlinear programming, *Math. Program.*, *89*(1), 149–185, doi:10.1007/PL00011391.

Carpenter, D. M. (1993), The lake effect of the Great Salt Lake: Overview and forecast problems, *Weather Forecasting*, *8*(2), 181–193, doi: 10.1175/1520-0434(1993)008¡0181:TLEOTG¿2.0.CO;2.

Chen, F., and J. Dudhia (2001), Coupling an advanced land surface-hydrology model with the Penn State-NCAR MM5 Modeling System. Part I: Model implementation and sensitivity, *Mon. Weather Rev.*, *129*(4), 569–585, doi:10.1175/1520-0493(2001)129¡0569: CAALSH¿2.0.CO;2.

Collins, W. D., et al. (2006), The community climate system model version 3 (CCSM3), *J. Clim.*, *19*(11), 2122–2143, doi:10.1175/JCLI3761.1.

Crosman, E., and J. Horel (2012), Idealized large-eddy simulations of sea and lake breezes: Sensitivity to lake diameter, *heat flux and stability*, *Boundary Layer Meteorol.*, *144*(3), 309–328.

Crosman, E. T., and J. D. Horel (2009), MODIS-derived surface temperature of the Great Salt Lake, *Remote Sens. Environ.*, *113*(1), 73–81, doi:10.1016/j.rse.2008.08.013.

Deng, B., S. Liu, W. Xiao, W. Wang, J. Jin, and X. Lee (2013), Evaluation of the CLM4 lake model at a large and shallow freshwater lake*, *J. Hydrometeorol.*, *14*(2), 636–649, doi:10.1175/JHM-D-12–067.1.

Ek, M. B., K. E. Mitchell, Y. Lin, E. Rogers, P. Grunmann, V. Koren, G. Gayno, and J. D. Tarpley (2003), Implementation of Noah land surface model advances in the National Centers for Environmental Prediction operational mesoscale Eta model, *J. Geophys. Res.*, *108*(D22), 8851, doi:10.1029/2002JD003296.

Fairall, C. W., E. F. Bradley, D. P. Rogers, J. B. Edson, and G. S. Young (1996), Bulk parameterization of air-sea fluxes for Tropical Ocean-Global Atmosphere Coupled-Ocean Atmosphere Response Experiment, *J. Geophys. Res.*, *101*(C2), 3747–3764.

Geleyn, J.-F., and A. Hollingsworth (1979), An economical analytical method for the computation of the interaction between scattering and line absorption of radiation, *Contrib. Atmos. Phys.*, *52*, 1–16.

Goyette, S., N. McFarlane, and G. M. Flato (2000), Application of the Canadian regional climate model to the Laurentian great lakes region: Implementation of a lake model, *Atmos. Ocean*, *38*(3), 481–503, doi:10.1080/07055900.2000.9649657.

Grim, J. A., J. C. Knievel, and E. T. Crosman (2013), Techniques for using MODIS data to remotely sense lake water surface temperatures, *J. Atmos. Oceanic Technol.*, *30*(10), 2434–2451, doi:10.1175/JTECH-D-13-00003.1.

Gula, J., and W. R. Peltier (2012), Dynamical downscaling over the Great Lakes Basin of North America using the WRF regional climate model: The impact of the great lakes system on regional greenhouse warming, *J. Clim.*, *25*(21), 7723–7742, doi:10.1175/JCLI-D-11-00388.1.

Hostetler, S. W., G. T. Bates, and F. Giorgi (1993), Interactive coupling of a lake thermal model with a regional climate model, *J. Geophys. Res.*, *98*(D3), 5045–5057, doi:10.1029/92JD02843.

Iziomon, M., H. Mayer, and A. Matzarakis (2003), Downward atmospheric longwave irradiance under clear and cloudy skies: Measurement and parameterization, *J. Atmos. Sol. Terr. Phys.*, *65*(10), 1107–1116, doi:10.1016/j.jastp.2003.07.007.

Kourzeneva, E., E. Martin, Y. Batrak, and P. L. Moigne (2012), Climate data for parameterisation of lakes in Numerical Weather Prediction models, *Tellus, Ser. A*, *64*, 17226, doi:10.3402/tellusa.v64i0.17226.

Leon, L., D. Lam, W. Schertzer, D. Swayne, and J. Imberger (2007), Towards coupling a 3D hydrodynamic lake model with the Canadian Regional Climate Model: Simulation on Great Slave Lake, *Environ. Modell. Software*, *22*(6), 787–796, doi:10.1016/j.envsoft.2006.03.005.

Ljungemyr, P., N. Gustafsson, and A. Omstedt (1996), Parameterization of lake thermodynamics in a high-resolution weather forecasting model, *Tellus, Ser. A*, *48*(5), 608–621.

MacKay, M. D., et al. (2009), Modeling lakes and reservoirs in the climate system, *Limnol. Oceanogr. Methods*, *54*, 2315–2329.

Martynov, A., L. Sushama, and R. Laprise (2010), Simulation of temperate freezing lakes by one-dimensional lake models: Performance assessment for interactive coupling with regional climate models, *Boreal Environ. Res.*, *15*, 143–164.

Mironov, D. (2008), Parameterization of lakes in numerical weather prediction: Description of a lake model, *Tech. Rep. 11*, 41 pp., Consortium for Small-scale Modelling, Offenbach am Main, Germany.

Mironov, D., L. Rontu, E. Kourzeneva, and A. Terzhevik (2010), Towards improved representation of lakes in numerical weather prediction and climate models: Introduction to the special issue of Boreal Environment Research, *Boreal Environ. Res.*, *15*, 97–99.

Naftz, D., C. Angeroth, M. Freeman, R. Rowland, and G. Carling (2013), Monitoring change in Great Salt Lake, *Eos Trans. AGU*, *94*(33), 289–290, doi:10.1002/2013EO330001.

Newby, J. E. (1980), Great Salt Lake railroad crossing, *Utah Geol. Miner. Surv. Bull.*, *116*, 393–400.

Notaro, M., K. Holman, A. Zarrin, E. Fluck, S. Vavrus, and V. Bennington (2012), Influence of the Laurentian Great Lakes on regional climate, *J. Clim.*, *26*(3), 789–804, doi:10.1175/JCLI-D-12–00140.1.

O'Gorman, P. A., and C. J. Muller (2010), How closely do changes in surface and column water vapor follow Clausius-Clapeyron scaling in climate change simulations?, *Environ. Res. Lett.*, *5*(2), 025207.

Onton, D. J., and W. J. Steenburgh (2001), Diagnostic and sensitivity studies of the 7 December 1998 Great Salt Lake-effect snowstorm, *Mon. Weather Rev.*, *129*(6), 1318–1338, doi:10.1175/1520-0493(2001)129¡1318:DASSOT¿2.0.CO;2.

Pokhrel, Y., N. Hanasaki, S. Koirala, J. Cho, P. J.-F. Yeh, H. Kim, S. Kanae, and T. Oki (2012), Incorporating anthropogenic water regulation modules into a land surface model, *J. Hydrometeorol.*, *13*(1), 255–269, doi:10.1175/JHM-D-11–013.1.

Price, J. F., R. A. Weller, and R. Pinkel (1986), Diurnal cycling: Observations and models of the upper ocean response to diurnal heating, cooling, and wind mixing, *J. Geophys. Res.*, *91*(C7), 8411–8427.

Raisanen, P. (1998), Effective longwave cloud fraction and maximum-random overlap of clouds: A problem and a solution, *Mon. Weather Rev.*, *126*(12), 3336–3340, doi:10.1175/1520-0493(1998)126¡3336:ELCFAM¿2.0.CO;2.

Ramamurthy, P., and E. R. Pardyjak (2011), Toward understanding the behavior of carbon dioxide and surface energy fluxes in the urbanized semi-arid Salt Lake Valley, Utah, USA, *Atmos. Environ.*, *45*, 73–84.

Rasmussen, R., et al. (2011), High-resolution coupled climate runoff simulations of seasonal snowfall over Colorado: A process study of current and warmer climate, *J. Clim.*, *24*(12), 3015–3048, doi:10.1175/2010JCLI3985.1.

Saha, S., et al. (2010), The NCEP climate forecast system reanalysis, *Bull. Am. Meteorol. Soc.*, *91*(8), 1015–1057.

Sahoo, G., and S. Schladow (2008), Impacts of climate change on lakes and reservoirs dynamics and restoration policies, *Sustainability Sci.*, *3*, 189–199.

Sahoo, G., S. Schladow, J. Reuter, R. Coats, M. Dettinger, J. Riverson, B. Wolfe, and M. Costa-Cabral (2013), The response of Lake Tahoe to climate change, *Climatic Change*, *116*(1), 71–95.

Schneider, E. K., and Z. Zhu (1998), Sensitivity of the simulated annual cycle of sea surface temperature in the equatorial Pacific to sunlight penetration, *J. Clim.*, *11*(8), 1932–1950, doi:10.1175/1520-0442-11.8.1932.

Schneider, P., and S. J. Hook (2010), Space observations of inland water bodies show rapid surface warming since 1985, *Geophys. Res. Lett.*, *37*, L22405, doi:10.1029/2010GL045059.

Shaviv, N. J. (2008), Using the oceans as a calorimeter to quantify the solar radiative forcing, *J. Geophys. Res.*, *113*, A11101, doi:10.1029/2007JA012989.

Skamarock, W. C., J. B. Klemp, J. Dudhia, D. O. Gill, D. M. Barker, W. Wang, and J. G. Powers (2005), A description of the advanced research WRF version 2, *NCAR Tech. Note TN-468 STR*, 88 pp., *Natl. Center for Atmos. Res.*, Boulder, Colo.

Small, E. E., L. C. Sloan, S. Hostetler, and F. Giorgi (1999), Simulating the water balance of the Aral Sea with a coupled regional climate-lake model, *J. Geophys. Res.*, *104*(D6), 6583–6602.

Steenburgh, W. J., and D. J. Onton (2001), Multiscale analysis of the 7 December 1998 Great Salt Lake-effect snowstorms, *Mon. Weather Rev.*, *129*(6), 1296–1317, doi:10.1175/1520-0493(2001)129¡1296:MAOTDG¿2.0.CO;2.

Steenburgh, W. J., S. F. Halvorson, and D. J. Onton (2000), Climatology of Lake-effect snowstorms of the Great Salt Lake, *Mon. Weather Rev.*, *128*(3), 709–727, doi:10.1175/1520-0493(2000)128¡0709:COLESO¿2.0.CO;2.

Subin, Z. M., W. J. Riley, and D. Mironov (2012), An improved lake model for climate simulations: Model structure, evaluation, and sensitivity analyses in CESM1, *J. Adv. Model. Earth Syst.*, *4*, M02001, doi:10.1029/2011MS000072.

Sun, H., R. Feistel, M. Koch, and A. Markoe (2008), New equations for density, entropy, heat capacity, and potential temperature of a saline thermal fluid, *Deep Sea Res., Part I*, *55*(10), 1304–1310, doi:10.1016/j.dsr.2008.05.011.

Thompson, G., P. R. Field, R. M. Rasmussen, and W. D. Hall (2008), Explicit forecasts of winter precipitation using an improved bulk microphysics scheme. Part II: Implementation of a new snow parameterization, *Mon. Weather Rev.*, *136*(12), 5095–5115, doi:10.1175/2008MWR2387.1.

Tsuang, B.-J., C.-Y. Tu, and K. Arpe (2001), Lake parameterization for the climate models, *Tech. Rep. 316*, Max Planck Inst. for Meteorol., Hamburg, Germany.

U.S. Geological Survey (2013), National water information system data available on the World Wide Web (USGS water data for the nation), Salt Lake City, Utah. [Available at http://waterdata.usgs.gov/nwis/, last accessed Sep 18, 2013.]

Yeager, K. N., W. J. Steenburgh, and T. I. Alcott (2012), Contributions of lake-effect periods to the cool-season hydroclimate of the Great Salt Lake Basin, *J. Appl. Meteorol. Climatol.*, *52*(2), 341–362, doi:10.1175/JAMC-D-12-077.1.

Zhao, L., J. Jin, S.-Y. Wang, and M. B. Ek (2012), Integration of remote-sensing data with WRF to improve lake-effect precipitation simulations over the Great Lakes region, *J. Geophys. Res.*, *117*, D09102, doi:10.1029/2011JD016979.

Zumpfe, D. E., and J. D. Horel (2007), Lake-breeze fronts in the Salt Lake Valley, *J. Appl. Meteorol. Climatol.*, *46*(2), 196–211, doi:10.1175/JAM2449.1.